General study of chameleon fifth force in gravity space experiments

Martin Pernot-Borràs, Joel Bergé, Philippe Brax, Jean-Philippe Uzan

General study of chameleon fifth force in gravity space experiments

Martin Pernot-Borràs,[1,2,*] Joel Bergé,[1] Philippe Brax,[3] and Jean-Philippe Uzan[2,4]

[1]*DPHY, ONERA, Université Paris Saclay, F-92322 Châtillon, France*
[2]*Institut d'Astrophysique de Paris, CNRS UMR 7095, Sorbonne Université, 98 bis Bd Arago, 75014 Paris, France*
[3]*Institut de Physique Théorique, Université Paris-Saclay, CEA, CNRS, F-91191 Gif-sur-Yvette Cedex, France*
[4]*Sorbonne Université, Institut Lagrange de Paris, 98 bis, Bd Arago, 75014 Paris, France*

(Received 30 July 2019; published 2 October 2019)

In this article we investigate the profile of the scalar field of a scalar-tensor theory subject to the chameleon mechanism in the context of gravity space missions like the MICROSCOPE experiment. We analyze the experimental situations for models with an inverse power-law potential that can in principle induce a fifth force inside the satellite, and hence either be detected or constrained. As the mass of the scalar field depends on the local matter density, the screening of the scalar field depends crucially on both the parameters of the theory (potential and nonminimal coupling to matter) and the geometry of the satellite. We calculate the profile of the scalar field in one-, two- and three-dimensional satellite configurations without relying on the thick- or thin-shell approximations for the scalar field. In particular, we consider the typical geometry with nested cylinders which is close to the MICROSCOPE design. In this case we evaluate the corresponding fifth force on a test body inside the satellite. This analysis clarifies previous claims on the detectability of the chameleon force by space-borne experiments.

DOI: 10.1103/PhysRevD.100.084006

I. INTRODUCTION

General relativity (GR) has successfully passed all experimental tests from the Solar System scale [1] to cosmology [2], including the recent confirmation of the existence and properties of gravitational waves [3,4]. However, GR has to be endowed with a dark sector (including dark matter and a cosmological constant) to provide a cosmological model consistent with observations [5,6]. The absence of convincing models for the dark sector has revived the interest for gravity theories beyond GR [1,7]. These theories introduce new degrees of freedom, the effects of which need to be suppressed on small scales, although they may play an important role on cosmological scales.

The simplest extension of GR posits the existence of a nonminimally coupled scalar field. Such a theory, with only one extra degree of freedom, involves at least two free functions (a potential and a universal coupling function when enforcing the weak equivalence principle). These scalar-tensor theories are currently well constrained from local scales observations [1,8] to cosmology [9,10]. When the potential and the coupling function enjoy the same minimum these theories can exhibit a cosmological attraction mechanism toward GR in such a way that they are in agreement with local experimental constraints [11]. The new degree of freedom can then be considered as a valid dark-energy candidate [12].

On small scales, the scalar field is responsible for a fifth force that has to be shielded in order to pass existing experimental tests. Several screening mechanisms have been proposed in the case of scalar-tensor theories, including the least coupling principle [13], the symmetron [14], and the chameleon mechanism [15,16]. The latter model assumes that the coupling and potential functions do not have the same minimum. It follows that the minimum of the effective potential depends on the local density of matter. Hence, in high-density environments, the field is heavier and the fifth force may have a range that is too small to be detected, while in low-density environments the fifth force can be long ranged.

Local gravity experiments on the existence of a fifth force already provide strong constraints on the existence of the chameleon field [17,18] (see Sec. VI D). The main bounds typically come from atom interferometry [19,20], Casimir effect measurements [21], or torsion balance experiments to detect short-scale forces [22]. Other efforts could lead to new advances by improving sensitivity or by imagining more original signatures [23]. It was originally expected [15,16] that space-based experiments could be highly competitive, as they would be performed in a lower-density environment.

However, all of these experiments suffer from the problem that their setups can screen the fifth force. The

*martin.pernot_borras@onera.fr

recent results on the test of the weak equivalence principle by the MICROSCOPE mission [24] orbiting the Earth have long been expected to provide new constraints on chameleon theories (as argued in Refs. [15,16]). In this experiment, even with a universal coupling, the proof masses can show different screenings of the field, leading to different accelerations. As a consequence, one would expect the equivalence principle to be violated for macroscopic extended objects, while it still holds at the fundamental level. The question is thus to determine how screened the chameleon field is at the level of a proof mass under the influence of the geometry of a given experiment, a study that has not been performed so far and for which this article is a first step. This is an intricate problem as the distribution of matter is often complex and the chameleon's dynamics is highly nonlinear. Most of the experiments cited above typically consist of a vacuum cavity enclosed in a shield that can contain experimental devices, such as electrodes or test masses. As these test masses are extended bodies, they must be taken into account in the profile of the field when computing the force they experience.

Two kinds of effects are expected depending on whether a cavity can be considered isolated or not. On the one hand, in the so-called "thin-shell" regime, the field inside the cavity is decoupled from the exterior since the cavity walls exponentially damp the field on a scale smaller than their thickness; in this case, the force applied to a test mass inside the cavity is local and is mostly determined by the structure and geometry of the cavity. On the other hand, in the so-called "thick-shell" regime, the exterior field can penetrate the cavity as it is marginally influenced by the matter constituting the cavity. The limit between these two regimes depends on the model parameters and the geometry of the experiments. In this article, we shall investigate these two dependences and compute the force exerted on a test mass in different settings.

To this end, we must determine the chameleon profile inside the experiment. This is a complex problem mostly because of the structure of the boundary conditions and the attraction of the profile toward a fixed point. It has been addressed in various ways in the literature. Analytic models suffer from the nonlinearities of the chameleon equation; to overcome them, the Klein-Gordon equation is often approximated by neglecting some terms or by linearizing the chameleon potential [16,21,25–32]. Numerical models [22,33–36] suffer from the limited resources they have, leading to solving the equation in a bounded region, setting the boundary conditions at a finite distance, or neglecting some short-scale variations of the field. Besides the fact that this last point may lead to an incorrect field even where the field varies slowly, this is very problematic for experiments using extended test masses. Short-scale variations are indeed more likely to happen in matter, impacting the very gradient responsible for the force that is being measured. This caveat is also encountered in analytic approaches.

This article overcomes these approximations. We tackle the problem numerically and consider all of the terms in the chameleon equation. To comply with the necessity to set boundary conditions at infinity, we consider a low-density background environment in which we embed a high-density system whose complexity increases throughout the paper. Our final goal is to approach the concentric-cylinder geometry of the MICROSCOPE instrument [24]. Although we restrict ourselves to static configurations with symmetries that are simpler than those in realistic cases, this paper will pave the way to further studies that include asymmetries and dynamics. We should note that most configurations studied in this article have already been partly explored in the literature, whether in specific regimes or with assumed boundary conditions. Here we investigate general profiles to clarify the boundary condition problem and to infer robust criteria to legitimize the approximations encountered in the literature.

This article is organized as follows. The first part of the paper focuses on one-dimensional (1D) geometries. In Sec. II, we discuss the dynamics of the chameleon field, paying particular attention to the role of boundary conditions. In Sec. III we analyze the case of an infinite wall, and in Sec. IV we consider the case of a one-dimensional cavity. Following these 1D configurations, we explore two-dimensional (2D) and three-dimensional (3D) symmetrical configurations in Sec. V. Finally, in Sec. VI we notice that the exact numerical integration of the field profile in a cavity leads to discrepancies with the analytic approximations used to evaluate the Casimir pressure induced by the chameleon field. We also consider the effect of the chameleon force on the motion of atoms in a cavity and the corresponding drift time, which could serve as a testing ground for such models. Finally, we present the field profile in nested cylindrical configurations close to the MICROSCOPE setting as a first step toward a more thorough investigation of the constraints from MICROSCOPE on chameleons, which is left for future work. We conclude in Sec. VII.

II. THE CHAMELEON'S PROFILE AND INITIAL CONDITIONS

A. Theoretical model

The chameleon mechanism is given in the Einstein frame by

$$S = \int \mathrm{d}x^4\sqrt{-g}\left[\frac{\mathrm{M}_{\mathrm{Pl}}^2}{2}R - \frac{1}{2}\partial^\mu\partial_\mu\phi - V(\phi)\right] - \int \mathrm{d}^4x\mathcal{L}_{\mathrm{m}}(\tilde{g}_{\mu\nu}, \psi_{\mathrm{matter}}, \ldots), \quad (1)$$

where ϕ is the chameleon field, V is its potential, M_{Pl} is the reduced Planck mass, R is the Ricci scalar, $g_{\mu\nu}$ is the Einstein frame metric, g is its determinant, and $\mathcal{L}_{\mathrm{m}}$ is the

matter Lagrangian with $\psi_{\rm matter}$ the matter fields. The field couples nonminimally to matter through the Jordan frame $\tilde{g}_{\mu\nu} = A^2(\phi) g_{\mu\nu}$, where A is a universal coupling function. We define the dimensionless coupling constant $\beta = \mathrm{M_{Pl}} \frac{\mathrm{d}\ln A}{\mathrm{d}\phi}$. The field could have different coupling functions for each component of matter, but here we restrict to a universal coupling.

For static configurations of nonrelativistic matter, the field follows the Klein-Gordon equation

$$\nabla^2\phi = V_{\mathrm{eff},\phi} \equiv V_{,\phi} + \frac{\beta}{\mathrm{M_{Pl}}}\rho_{\rm mat}, \tag{2}$$

where $\rho_{\rm mat}$ is the mass density function. For nonstatic configurations, the Laplacian would be a d'Alembertian. We use the Ratra-Peebles inverse power-law potential of energy scale Λ and exponent n [17,37] as a typical example of a chameleon model,

$$V(\phi) = \Lambda^4\left(1 + \frac{\Lambda^n}{\phi^n}\right). \tag{3}$$

The effective potential $V_{\rm eff}$ has a minimum given by

$$\phi_{\rm min}(\rho_{\rm mat}) = \left(\mathrm{M_{Pl}}\frac{n\Lambda^{n+4}}{\beta\rho_{\rm mat}}\right)^{\frac{1}{n+1}}. \tag{4}$$

It plays a central role in the chameleon dynamics.

We recall that in a medium with constant density, the field is expected to relax exponentially to the minimum of its potential. It varies on a typical scale of the order of its local Compton wavelength,

$$\lambda_{\rm c}(\rho_{\rm mat}) \equiv m^{-1}(\rho_{\rm mat}) = \frac{1}{\sqrt{V''_{\rm eff}(\phi_{\rm min})}}, \tag{5}$$

which is explicitly given, in the models considered in this article, by

$$\lambda_{\rm c}(\rho_{\rm mat}) = \sqrt{\frac{1}{n(n+1)\Lambda^{n+4}}\left(\frac{n\mathrm{M_{Pl}}\Lambda^{n+4}}{\beta\rho_{\rm mat}}\right)^{\frac{n+2}{n+1}}}. \tag{6}$$

The fifth force induced by the coupling to the chameleon field on a test point mass is proportional to the gradient of the scalar field and given by

$$\vec{F} = -\frac{\beta}{\mathrm{M_{Pl}}} m_{\rm test}\vec{\nabla}\phi. \tag{7}$$

Nevertheless an extended body cannot *a priori* be considered as a test body since its own matter density impacts the field profile inside and outside its volume. Hence, to properly evaluate the force one needs to solve consistently for the field profile including the extended body and integrate this force over the whole volume of the body.

In what follows, it is convenient to rewrite the chameleon's Klein-Gordon equation (2) in terms of $\phi_{\rm min}$ as

$$\nabla^2\phi = n\Lambda^{n+4}\left[\frac{1}{\phi_{\rm min}^{n+1}(\rho_{\rm mat})} - \frac{1}{\phi^{n+1}}\right], \tag{8}$$

where the dependence on the local mass density is now contained in $\phi_{\rm min}$.

If we consider a region of space with local density $\rho_{\rm vac}$ that is large compared to the corresponding chameleon's Compton wavelength and far from any perturbing body, we can assume that the field is uniform with a value $\phi_{\rm vac} = \phi_{\rm min}(\rho_{\rm vac})$. We shall now study the way a one-dimensional material structure affects this uniform profile as experiencing the different $\phi_{\rm min}$ associated to the different environments the field should depart from $\phi_{\rm vac}$.

B. Initial conditions in one dimension

The chameleon profile is a solution to a boundary value problem. Given the previous discussion, the field shall relax to its minimum value in the external space, such that

$$\begin{cases} \phi \xrightarrow[x\to+/-\infty]{} \phi_{\rm min}(\rho_{\rm vac}), \\ \phi' \xrightarrow[x\to+/-\infty]{} 0. \end{cases} \tag{9}$$

Such a boundary value problem can be solved using finite-difference methods. However, due to the finite extent of computational memory we cannot set boundary conditions at infinity. We then need to set the boundary conditions at a finite distance from the considered object, and make a compromise between computational memory limits and the distance at which we can consider that the gap between the value that the field takes and $\phi_{\rm vac}$ becomes negligible. The Compton wavelength in vacuum $\lambda_{\rm c,vac}$ is an estimate of this distance [16,17]. This is an approximate criterion; a more accurate one will be determined in the following by the direct integration of an initial value problem.

Initial conditions cannot be chosen to be at $\phi_{\rm vac}$ with a null derivative. To understand this we must note the key role played by $\phi_{\rm min}$ as a fixed point of the theory. One can check that for $n > 0$ we have

$$\frac{\mathrm{d}^2\phi}{\mathrm{d}x^2}\begin{cases} > 0 & \text{if } \phi > \phi_{\rm min}, \\ = 0 & \text{if } \phi = \phi_{\rm min}, \\ < 0 & \text{if } \phi < \phi_{\rm min}, \end{cases} \tag{10}$$

so that the field derivative increases (decreases) for $\phi > \phi_{\rm min}$ ($\phi < \phi_{\rm min}$). For $\phi = \phi_{\rm min}$, the field's derivative will not vary.

Hence, if we choose the initial conditions $\phi'_{\rm i} = 0$, as in Fig. 1, the field will diverge monotonically toward $+\infty$ or $-\infty$ at large x, for an initial value $\phi_{\rm i} > \phi_{\rm min}$ or $\phi_{\rm i} < \phi_{\rm min}$, respectively. For an initial value $\phi_{\rm i} = \phi_{\rm min}$, since $\phi_{\rm min}$ is a fixed point the field remains constant.

If we choose $\phi'_{\rm i} \neq 0$, the considerations in Eq. (10) do not change and the ϕ' evolution remains the same. Nevertheless,

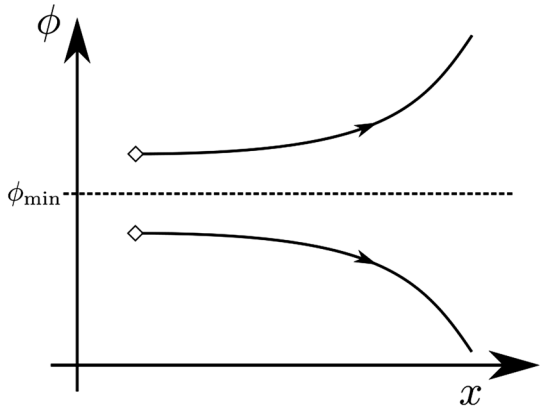

FIG. 1. Sketch of the field profiles for null initial derivatives: $\phi_{\rm i}' = 0$. Different behaviors are obtained depending on the magnitude of $\phi_{\rm i}$ compared to $\phi_{\rm min}$.

the field evolution will no longer be monotonic and will eventually show maxima and minima. In the case where $\phi_{\rm i} > \phi_{\rm min}$, if $\phi_{\rm i}' > 0$, the field will diverge more rapidly than if $\phi_{\rm i}' = 0$, if $\phi_{\rm i} < 0$, new behaviors will occur. The different possible evolutions for $\phi_{\rm i}' \neq 0$ are sketched in Fig. 2. For small values of $|\phi_{\rm i}'|$, the field does not have enough "speed" to reach $\phi_{\rm min}$, and thus it will reach a minimum and then diverge. For high values of $|\phi_{\rm i}'|$, the field can reach $\phi_{\rm min}$. When crossing $\phi_{\rm min}$, ϕ' will still be negative, but as we now have $\phi < \phi_{\rm min}$ it will decrease and make the field diverge negatively. For a given $\phi_{\rm i}$, there is only one value of $\phi_{\rm i}'$ (in between these two behaviors) that will cause ϕ' to vanish precisely when the field reaches $\phi_{\rm min}$. In this case, $\phi_{\rm i}$ is fixed by the considered matter distribution.

Note that the case where $\phi_{\rm i} < \phi_{\rm min}$ is completely symmetric with the case where $\phi_{\rm i} > \phi_{\rm min}$, as shown by the light grey curves in Fig. 2.

In 1D, the problem can be treated relatively easily. The chameleon equation can indeed be integrated once, from

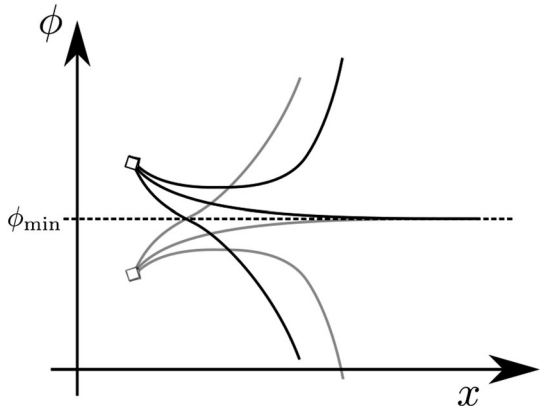

FIG. 2. Sketch of the field profiles for nonzero initial derivatives: $\phi_{\rm i}' \neq 0$. Different behaviors (each line) are obtained depending on the magnitude and sign of $\phi_{\rm i}'$. Grey lines correspond to $\phi_{\rm i} < \phi_{\rm min}$.

infinity—where boundary conditions are verified—to the place we want to set the initial conditions. This gives a condition on $\phi_{\rm i}'$ in terms of $\phi_{\rm i}$,

$$\frac{1}{2}\phi_{\rm i}'^2 = \frac{n}{\phi_{\rm vac}^{n+1}}(\phi_{\rm i} - \phi_{\rm vac}) + \left(\frac{1}{\phi_{\rm i}^n} - \frac{1}{\phi_{\rm vac}^n}\right). \quad (11)$$

This leaves us with only one initial parameter to deal with. We can use shooting methods, varying $\phi_{\rm i}$ to obtain the proper solution for the considered configuration.

III. EFFECT OF AN INFINITE WALL ON THE CHAMELEON'S DYNAMICS

A. An interface between two infinite domains

As a first step, we consider the simple case of an interface between two infinitely extended domains of different densities, for instance, a high-density wall and a low-density vacuum of density $\rho_{\rm wall}$ and $\rho_{\rm vac}$, respectively.

Far from the interface, the field will tend toward the value that minimizes the potential in each environment: $\phi_{\rm wall}$ and $\phi_{\rm vac}$, respectively. Note that Eq. (4) implies $\phi_{\rm vac} > \phi_{\rm wall}$. In between, the field will evolve smoothly and cross the interface with a value $\phi_{\rm I}$ and a continuous derivative, with $\phi_{\rm wall} < \phi_{\rm I} < \phi_{\rm vac}$. To solve for the profile numerically, we set the initial conditions at this interface. In the wall since $\phi_{\rm I} > \phi_{\rm wall}$, the profile is analogous to the case shown by the black line that asymptotically tends toward $\phi_{\rm min}$ in Fig. 2. In the other domain, the symmetric dotted line is more relevant, as now $\phi_{\rm I} < \phi_{\rm vac}$.

In this configuration, no shooting methods are required. This is because the asymptotic conditions on both sides of the interface give two different conditions [equivalent to Eq. (11)] on $\phi_{\rm I}$ and $\phi_{\rm I}'$, given by

$$\frac{1}{2}\phi_{\rm I}'^2 = \frac{n}{\phi_{\rm vac}^{n+1}}(\phi_{\rm I} - \phi_{\rm vac}) + \left(\frac{1}{\phi_{\rm I}^n} - \frac{1}{\phi_{\rm vac}^n}\right), \quad (12)$$

$$\frac{1}{2}\phi_{\rm I}'^2 = \frac{n}{\phi_{\rm wall}^{n+1}}(\phi_{\rm I} - \phi_{\rm wall}) + \left(\frac{1}{\phi_{\rm I}^n} - \frac{1}{\phi_{\rm wall}^n}\right). \quad (13)$$

Combining these two equations gives $\phi_{\rm I}$ and $\phi_{\rm I}'$ in terms of $\phi_{\rm wall}$ and $\phi_{\rm vac}$. We can then integrate numerically in both domains. Figure 3 depicts such a solution with the interface at $x = 0$. Note that for this profile and for every other profile computed in the following, if not stated otherwise, we consider the case where $n = 2$, $\beta = 1$, $\Lambda = 1$ eV, $\rho_{\rm wall} = 8.125\ {\rm g\,cm^{-3}}$, and $\rho_{\rm vac} = 10^{-3}\rho_{\rm wall}$ ($\phi_{\rm vac} = 10\phi_{\rm wall}$ for $n = 2$). In each domain, the field reaches the corresponding minimum of its potential within scales given by the Compton wavelength $\lambda_{\rm c}(\rho_{\rm mat})$. For the set of parameters and densities considered throughout the article, we have $\lambda_{\rm c,vac} \simeq 2$ m and $\lambda_{\rm c,wall} \simeq 0.02$ m. Note that for the sake of clarity, we chose $\rho_{\rm vac}$ and $\rho_{\rm wall}$ values that are not vastly different. For more realistic vacuum cavities, $\rho_{\rm vac} = 10^{-15}\rho_{\rm wall}$, implying a more significant difference between $\lambda_{\rm c,vac}$ and $\lambda_{\rm c,wall}$.

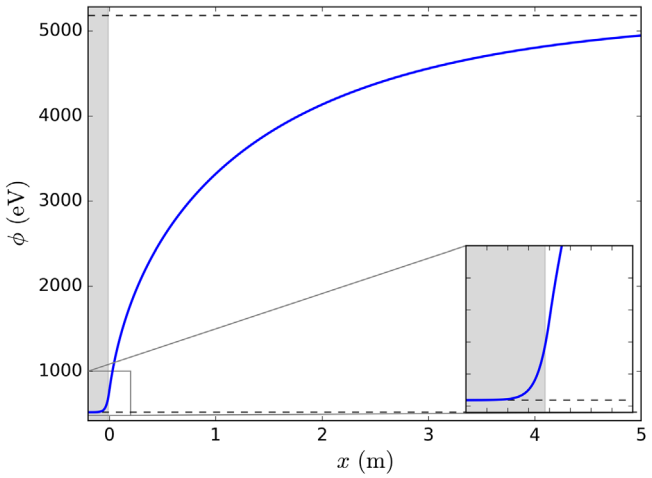

FIG. 3. Example of field profiles with an interface at $x = 0$. $\phi_{\rm min}$ values are shown with the two dashed lines. The grey zone is the higher density domain.

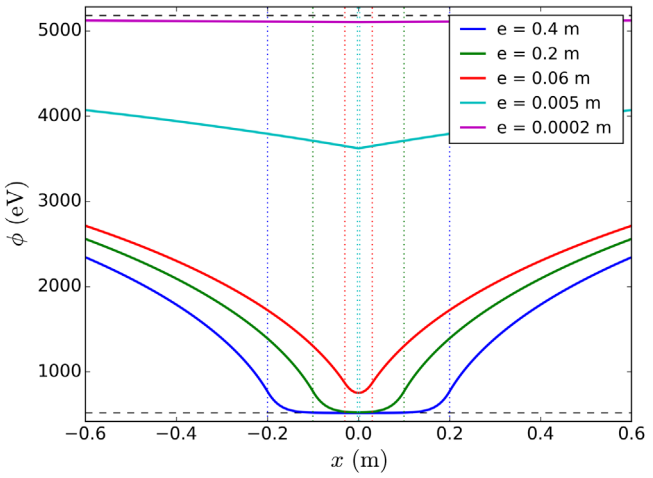

FIG. 4. Field profiles for different wall thicknesses e. The two values of $\phi_{\rm min}$ are shown by the two dashed lines. Dotted lines show the extent of the walls.

B. A single wall

We then consider a single wall of uniform density embedded in the low-density background environment. we denote its thickness by e. On both sides of the wall, the field will evolve similarly as in the previous section. We set the initial conditions on one of the borders of the wall, say, on the right side. We denote them by $\phi_{\rm e}$ and $\phi'_{\rm e}$. By symmetry, the field value will be the same on the other border of the wall, with a derivative of opposite sign. As in the previous section, we know that $\phi_{\rm wall} < \phi_{\rm e} < \phi_{\rm vac}$ with ${\phi_{\rm e}}' > 0$, and by direct integration the boundary conditions give a condition on $\phi'_{\rm e}$ in terms of $\phi_{\rm e}$,

$$\phi'_{\rm e} = \pm\sqrt{2\left[\frac{n}{\phi_{\rm vac}^{n+1}}(\phi_{\rm e} - \phi_{\rm vac}) + \left(\frac{1}{\phi_{\rm e}^{n}} - \frac{1}{\phi_{\rm vac}^{n}}\right)\right]}, \quad (14)$$

where we choose the positive sign in this case.

If we look toward the wall, the initial field derivative ${\phi_{\rm e}}'$ will look negative. As $\phi_{\rm e} > \phi_{\rm wall}$, the field will be similar to the black line that shows a minimum in Fig. 2. The field will then evolve from $\phi_{\rm e}$ to a minimum value reached at the center of the wall. The scale of this evolution will depend on the magnitude of $\phi_{\rm e}$. Consequently, there is a one-to-one mapping between e and $\phi_{\rm e}$: the larger the value of $\phi_{\rm e}$, the smaller the value of e.

Figure 4 depicts the numerical integration of a series of profiles for different values of e. Dotted lines delimit the frontiers of the considered wall. As expected, the thicker the wall gets, the more space the field has to evolve inside the wall, so the closer it gets to $\phi_{\rm wall}$.

1. $\phi_{\rm e}(e)$ relation

To compute the profile associated with any wall thickness we need to determine the relation $\phi_{\rm e}(e)$, which can be obtained by a shooting method. Figure 5 shows an example of such a relation for our fiducial parameters (n, β, Λ), and $\phi_{\rm wall}$, $\phi_{\rm vac}$.

This figure shows that a limited range for $\phi_e \in [\phi_{\rm I}, \phi_{\rm vac}]$ realizes all possible value of $e \in \mathbb{R}^+$. The bounds of this range are given by two limiting regimes:

(i) $\phi_{\rm vac}$ corresponds to the limiting case where the wall becomes infinitely thin and represents a very tiny perturbation to the background field.

(ii) $\phi_{\rm I}$ corresponds to the other limiting case where the field tends to reach $\phi_{\rm wall}$ at the center of the wall: we say that the field is completely screened inside the wall. The profile can be seen as two concatenated profiles of the case in Sec. III A, which explains the value $\phi_{\rm I}$ as the lower boundary. This behavior is consistent with the fact that the field is exponentially

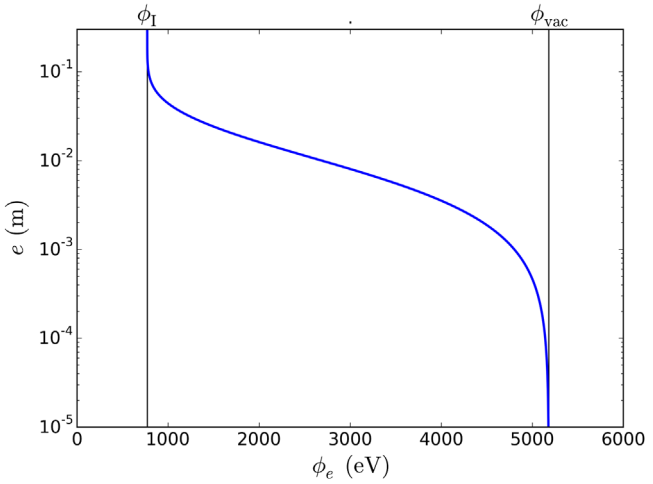

FIG. 5. Example of the relation $\phi_{\rm e}(e)$. The black lines denote $\phi_{\rm I}$ and $\phi_{\rm vac}$.

suppressed in the wall on scales of the Compton wavelength $\lambda_{\mathrm{c,wall}}$ in the wall.

2. $\phi_{\mathrm{e}}(e)$'s dependence on Λ and β

ϕ_{I} and ϕ_{vac} depend on Λ and β in such a way that the interval $[\phi_{\mathrm{I}}, \phi_{\mathrm{vac}}]$ spreads or shrinks. It spreads logarithmically with Λ and shrinks logarithmically with β. Figure 6 shows how the $\phi_{\mathrm{e}}(e)$ relation depends on Λ. Here the interval $[\phi_{\mathrm{I}}, \phi_{\mathrm{vac}}]$ is normalized to the interval [0, 1].

This figure shows that when varying Λ, the $\phi_{\mathrm{e}}(e)$ relations have the same slope, but are just shifted on the e axis. The dependence on β is similar, albeit in the opposite direction. To understand this variation, we can choose a specific value in the $[\phi_{\mathrm{I}}, \phi_{\mathrm{vac}}]$ interval, say, $\frac{\phi_{\mathrm{e}}-\phi_{\mathrm{I}}}{\phi_{\mathrm{vac}}-\phi_{\mathrm{I}}} = 0.5$, and see how e varies with Λ and β. We can fit this variation as

$$e(\Lambda, \beta) = A \times \Lambda \times \beta^{-\frac{2}{3}}, \tag{15}$$

where A is a coefficient that depends in a nontrivial way on ρ_{wall} and ρ_{vac}. In the cases considered in this figure, $\mathrm{A} = 2.15 \times 10^{-3}\ \mathrm{m\,eV^{-1}}$.

3. Screening of the wall

As mentioned before, when the wall gets thicker, it gets screened so that the field tends to the value that minimizes the potential inside the wall ϕ_{wall} at the center of the wall. In this case, we can consider that the field's dynamics on both sides of the wall decouple, such that if the matter distribution were to change on one side of the wall it would not influence the field on the other side. This will be important for the case of a cavity.

This was expected to happen for walls thicker than $\lambda_{\mathrm{c,wall}}$ [17]. Nevertheless, we can deduce from our simulations a more accurate criterion. We can indeed measure the

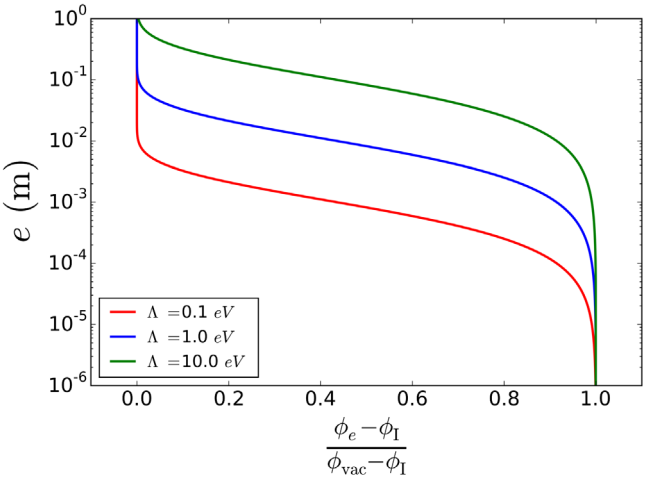

FIG. 6. Variation of $\phi_{\mathrm{e}}(e)$ with Λ, for $\Lambda = 0.1, 1, 10$ eV. The interval on which $\phi_{\mathrm{e}}(e)$ is defined is normalized to [0,1].

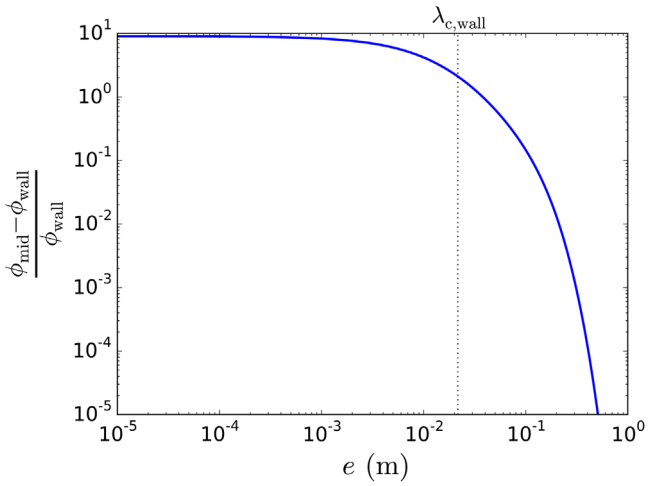

FIG. 7. Variation with the wall thickness e of the difference between the value of the field at the center of the wall and ϕ_{wall}.

difference between ϕ_{wall} and the effective minimum value the field reaches at the center of the wall. Figure 7 shows its evolution with the wall thickness.

As expected, we observe that this difference slowly decreases as the wall gets thicker. It then suddenly decreases when the wall thickness exceeds $\lambda_{\mathrm{c,wall}}$. We can consider that this gap becomes negligible when it reaches a thickness of roughly $100\lambda_{\mathrm{c,wall}}$, as it gets smaller than typical numerical precisions. This criterion is useful for other numerical methods such as finite-difference methods, in which one can only solve the field in a bounded region. For instance, when considering a system totally surrounded by walls, one can safely set initial conditions for the field to be at its minimum deeply inside these walls, as long as these walls have thicknesses greater than $100\lambda_{\mathrm{c,wall}}$.

4. Range of influence of a wall

We can also deduce the scale of influence of a wall. Outside the wall, the field slowly relaxes to its asymptotic value ϕ_{vac}.

The typical relaxation scale L_ϵ at which the gap between the field and ϕ_{vac} becomes negligible is given by

$$\frac{\phi(e/2 + L_\epsilon) - \phi_{\mathrm{vac}}}{\phi_{\mathrm{vac}}} = \epsilon, \tag{16}$$

where we take ϵ to be small. We can then consider that for distances to the wall larger than L_ϵ, the dynamics of the field is no longer influenced by the wall.

Figure 8 shows how this scale of influence varies with the wall thickness, for $\epsilon = 1\%$. We observe that it increases when the wall gets thicker, and finally reaches a plateau when the wall is totally screened, i.e., its thickness exceeds $\lambda_{\mathrm{c,wall}}$.

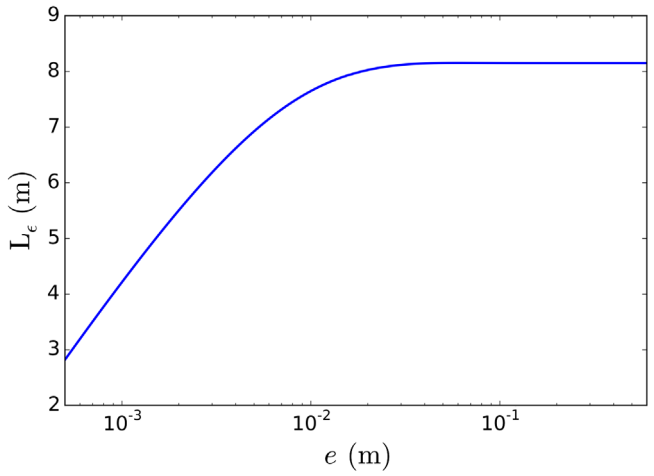

FIG. 8. Scale of influence L_ϵ of a wall as a function of e, for $\epsilon = 1\%$.

We can infer a useful criterion from such a figure. We can safely assume that the influence of the wall cannot be felt farther than $10\lambda_{c,vac}$ from it.

IV. ONE-DIMENSIONAL CAVITY

A. Profile and $\phi_d(d)$ relation

The experimental case of a cavity in one dimension is modeled as two walls of equal thickness e, separated by an empty space of size d, as illustrated in Fig. 9. For simplicity we assume that the cavity has the same density as the background environment ρ_{vac}.

We follow the same approach as in the previous section. We impose initial conditions at the external border of a wall, say, the right one. When fixing the thickness of the wall, the initial conditions will be determined by the size of the cavity d, so we denote them by ϕ_d and ϕ'_d. The same first integration in the external vacuum region gives a condition on ϕ'_d in terms ϕ_d to satisfy the boundary condition at infinity. The magnitude of ϕ_d determines the dynamics of the field inside the walls/cavity system. The overall profile will still be symmetric around the cavity center.

Inside the walls, the field is no longer symmetric. It must indeed reach a value smaller than ϕ_d on the inside border of the wall, as otherwise it would have the same asymptotic behavior as in the external vacuum region or diverge. Thus, if $\phi_e(e)$ is the initial value of the field given in the previous section for a wall of thickness e, we should now choose $\phi_d < \phi_e(e)$. In this way, the field will not have enough "speed" to reach ϕ_d again at the border of the cavity, but it will instead reach a value $\phi(d/2) < \phi_d < \phi_{vac}$, with a positive derivative. Then, in the cavity the field will have the same kind of dynamics with a maximum as for the bottom grey line in Fig. 2, and reach $\phi(d/2)$ again at the other side of the cavity.

For a fixed wall thickness e, ϕ_d will determine the value of $\phi(d/2)$, which will determine the maximum field

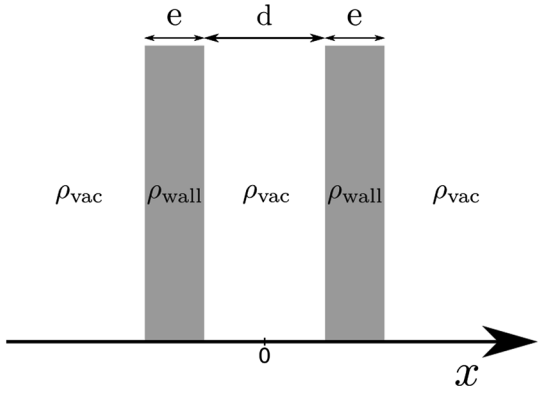

FIG. 9. 1D cavity.

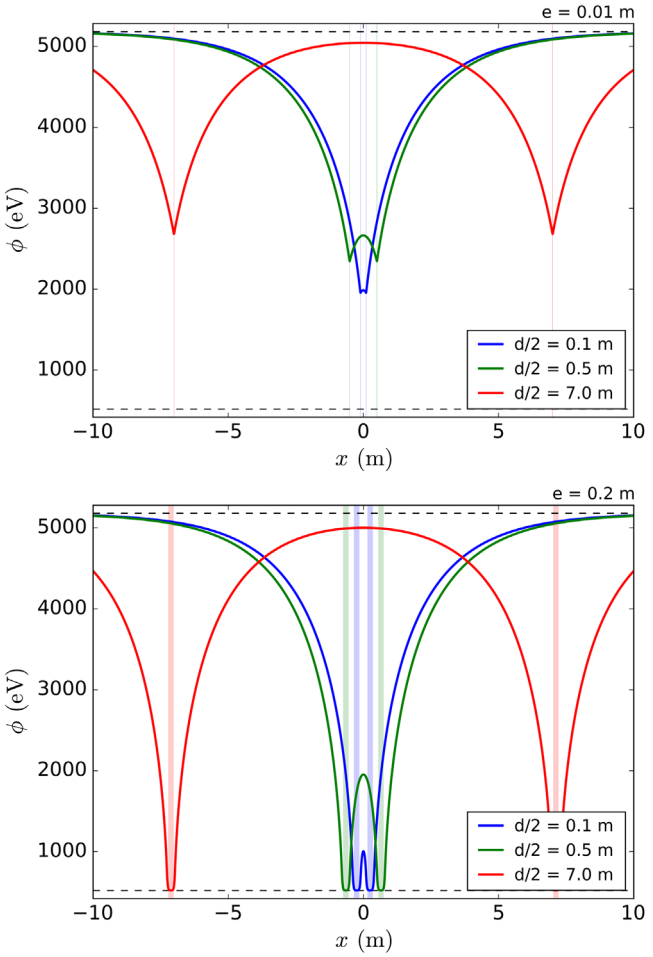

FIG. 10. Field profiles for different cavity sizes with unscreened (upper panel) and screened (lower panel) walls of thickness $e = 0.01$ m and $e = 0.2$ m, respectively. The values of ϕ_{min} are shown as dashed lines. The walls are represented by vertical colored strips.

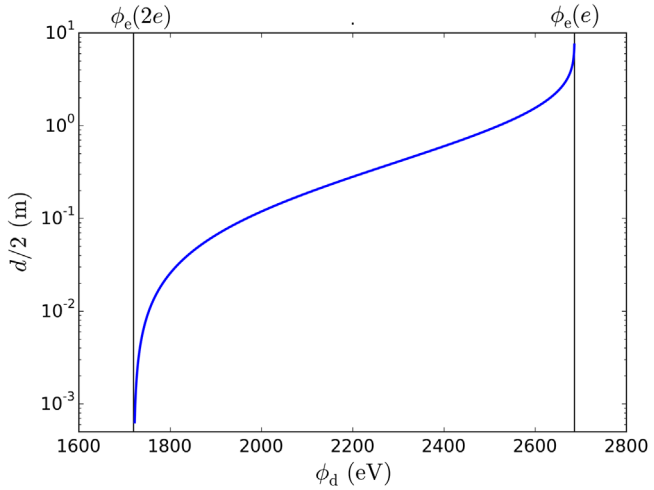

FIG. 11. Relation $\phi_e(d)$, for $e = 1$ cm. $\phi_{\min}$ values are shown with the two black lines.

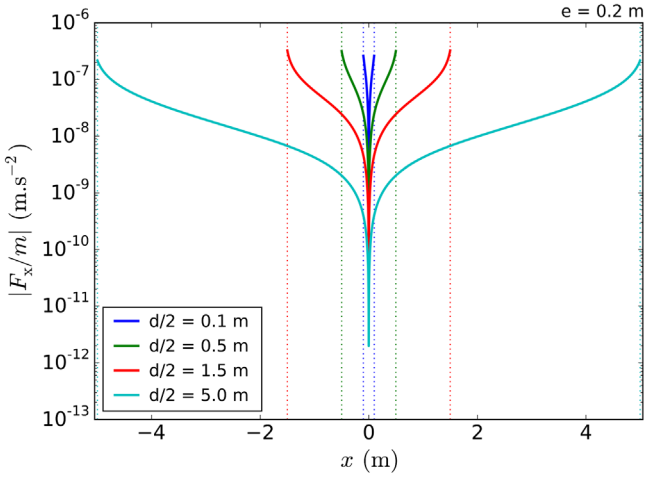

FIG. 12. Force experienced by a test mass for different cavity sizes, for screened walls with $e = 1$ m.

value ϕ_0 at the cavity center. Thus, we will obtain the corresponding cavity size d. We use the same shooting method as in the previous section to numerically determine how ϕ_d varies with d, and hence the $\phi_d(d)$ relation. Note that the larger the value of d, the larger the value of ϕ_0.

Figure 10 shows profiles corresponding to different cavity sizes, with a thin wall of size $e = 1$ cm (upper panel) and a thick screened wall of size $e = 20$ cm (lower panel). We find bubble profiles inside the cavity similar to Refs. [25,26].

Figure 11 shows an example of the $\phi_d(d)$ relation with thin unscreened walls of size $e = 1$ cm. As for the case of a single wall, the whole interval for $d \in \mathbb{R}$ is spanned by a restrained interval for ϕ_d, $[\phi_e(2e), \phi_e(e)]$, where $\phi_e(2e)$ corresponds to the initial condition associated with a single wall of size $2e$.

The curve for $\phi_d(d)$ is similar to $\phi_e(e)$ in the previous section, with two regimes. For $d \gg \lambda_{c,vac}$, the field has enough space in the cavity to reach a value ϕ_0 at its center close to the potential minimum ϕ_{vac}. In this regime, and as the cavity grows larger the two walls can be considered to be isolated, so the dynamics of the field is very similar to the one seen in Sec. III B. This explains why ϕ_d varies very slowly with d, with $\phi_d \simeq \phi_e(e)$.

On the other hand, as the size of cavity decreases the field has less and less space to evolve, such that ϕ_0 gets smaller. In this regime, as the two walls get closer, the dynamics of the field tends to the dynamics of a single wall of thickness $2e$. This explains why small values of d are obtained for ϕ_d tending towards $\phi_e(2e)$.

B. Chameleonic force in a cavity

Using the field profiles in a cavity, we can deduce the fifth force that a test point mass would feel using Eq. (7).

Figure 12 shows the magnitude of the fifth force experienced by a test mass inside cavities of different sizes for a constant wall thickness as expressed by Eq. (7). This force is directed outward. The wall is chosen here to be screened with $e = 0.2$ m. It shows that the force profile does not vary much, but just stretches with the cavity. The maximum force value reached at the border of the cavity varies slightly.

Conversely, Fig. 13 shows how the force profile changes as a function of the wall thickness, at constant cavity size. One can see that the magnitude of the force increases as the walls get thicker. In agreement with previous considerations, it stops varying when the wall thickness exceeds $\lambda_{c,wall} = 2.2$ cm, as the screened walls isolate the inner dynamics from the outside. Thus, larger forces are expected in cavities separated by thick walls. Nevertheless, in the case of thin walls, we expect it to be overtaken by effects sourced by external objects.

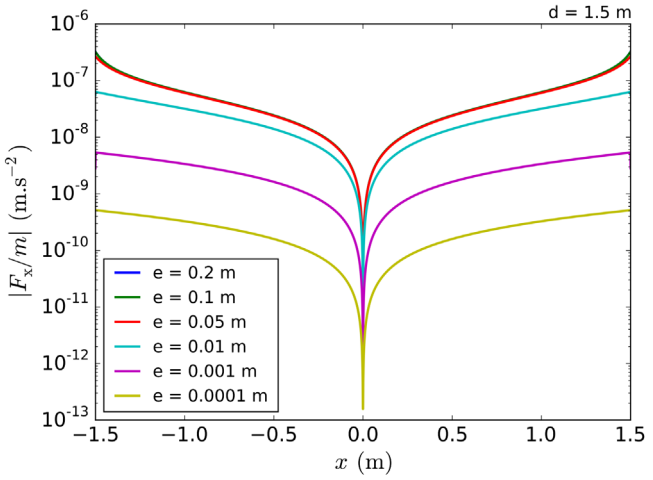

FIG. 13. Force experienced by a test mass for different wall sizes, for a fixed cavity size $d = 1.5$ m.

V. CYLINDRICAL AND SPHERICAL SYSTEMS

In 2D and 3D, the method previously used is no longer applicable. The chameleon's Klein-Gordon equation (8) indeed becomes in cylindrical or spherical symmetries

$$\frac{\mathrm{d}^2\phi}{\mathrm{d}r^2}+\frac{(D-1)}{r}\frac{\mathrm{d}\phi}{\mathrm{d}r}=n\Lambda^{n+4}\left[\frac{1}{\phi_{\mathrm{min}}^{n+1}(\rho_{\mathrm{mat}})}-\frac{1}{\phi^{n+1}}\right], \tag{17}$$

where D is the dimension of the symmetry. For $D \geq 2$, the first field's derivative term prevents us from obtaining a condition on the initial field derivative by integrating the chameleon equation once. Thus, we cannot follow the same scheme as before, and we need to adjust the two initials conditions ϕ_{i} and ϕ'_{i}.

Nevertheless, it is convenient to set the initial conditions at the symmetry center, as by symmetry the derivative of the field cancels. We thus have to determine a single parameter—the value of the field ϕ_0—to obtain the correct profile. A dichotomy algorithm can be used to determine the correct ϕ_0 that satisfies the correct asymptotic boundary conditions (9). A more complex analysis of the chameleon's dynamics than the one in Sec. II B shows that if the value of ϕ_0 is greater (weaker) than its correct value, the field will asymptotically diverge positively (negatively). Then, by solving the field for some ϕ_0, we can evaluate whether the field is greater or lesser than ϕ_{vac} at some large distance far greater than $\lambda_{\mathrm{c,vac}}$ from the considered system, and then adjust ϕ_0 as a dichotomy and reproduce the same procedure.

This converges rapidly toward the correct profile. It is important to note that, because the symmetry center is the origin of the coordinate system ($r = 0$), we cannot impose initial conditions at this point as the second term in Eq. (17) diverges numerically due to its dependence on r. We instead impose them very close to $r = 0$, with $\phi_{\mathrm{i}} = \phi_0$ and $\phi'_{\mathrm{i}} = 0$. This should lead to an error on the obtained field. The fields obtained in a 1D cavity with this method agree with the fields obtained with the previous method to less than 0.1%.

A. Cylindrical and spherical cavity

Analogously to Sec. IV, the cases of a cavity in 2D and 3D are, respectively, an infinitely extended cylinder and an empty sphere. Here we still denote the diameter of the cavity by d and the wall thickness by e.

The radial profiles in such cases are very similar to the 1D case. For equal cavity size, the effect of cylindrical and spherical symmetry decreases the values reached in the cavity. Figure 14 shows examples of radial profiles for 1D, 2D, and 3D cavities in the cases of screened walls and unscreened walls.

When the wall is screened the nature of the cavity does not affect the field outside. The field tends to reach lower values in the cavity for larger cavity sizes, leading to a weaker force. When the wall is not screened, the behavior becomes inverted and the size of the cavity has an impact on the exterior field.

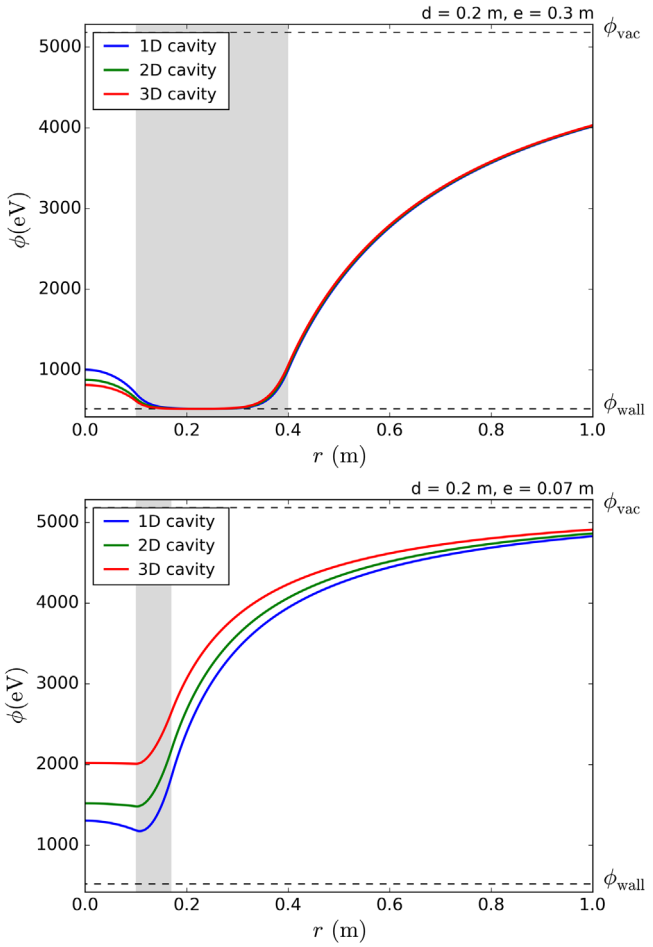

FIG. 14. Field profiles for 1D, 2D, and 3D cavities in the case of screened walls of thickness $e = 30$ cm and unscreened walls of thickness $e = 7$ cm. Values of ϕ_{min} are shown as dashed lines. The wall is shown by the grey region.

B. ϕ_0 variation

As for the 1D cavity, the larger the cavity, the larger the value of ϕ_0 reached by the field at the center of the cavity. In the literature (e.g., Ref. [16] for a sphere or Refs. [18,38] for a cylinder), this value was expected to be that of the field whose mass matches the radius of the cavity, i.e., that is given by

$$\frac{d}{2}=m^{-1}(\phi_0)=\frac{1}{\sqrt{V''(\phi_0)}}. \tag{18}$$

In Fig. 15 the value of ϕ_0 obtained with this approximate criterion is compared to the actual value given by these simulations for 1D, 2D, and 3D cavities. All curves have the same global monotony. Nevertheless, whereas simulations show that $\phi_0 \in [\phi_{\mathrm{wall}}, \phi_{\mathrm{vac}}]$, the approximated criterion does not give a bounded range for ϕ_0.

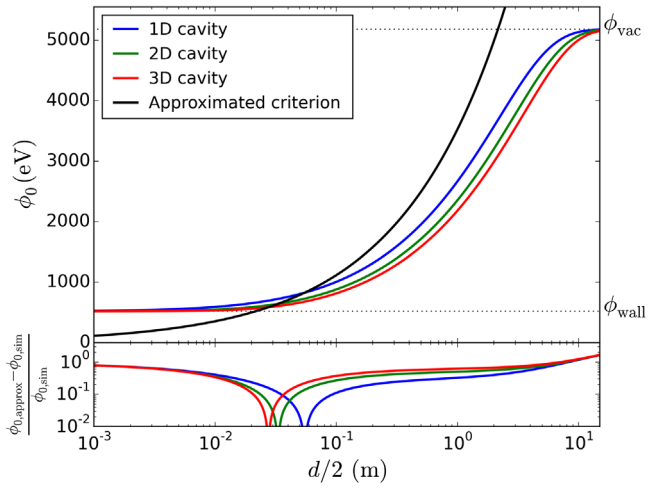

FIG. 15. Central value of the field in the cavity as a function of the cavity size d for screened walls of thickness $e = 0.1$ m. The colored lines correspond to 1D, 2D, and 3D cavities. The black line is an approximated estimation from Ref. [16]. $\phi_{\rm min}$ values are shown by the two dotted lines. The lower panel shows the relative difference between the two curves.

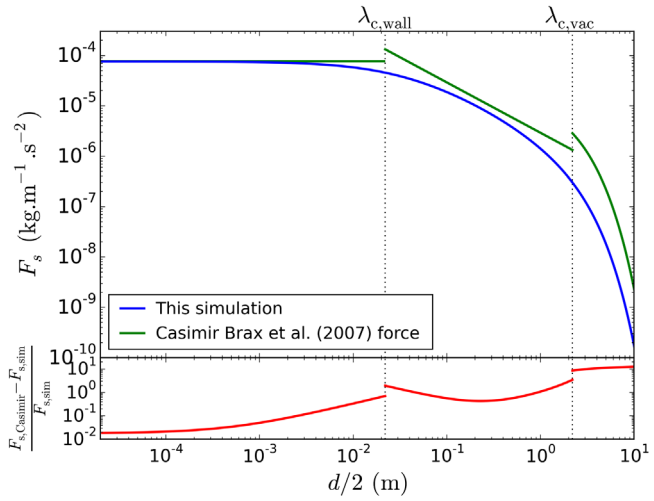

FIG. 16. Upper panel: chameleon-originated Casimir force as a function of the separation d of the walls for screened walls with $e = 0.2$ m. The blue curve is the result of this simulation. The green lines come from the analytical model of Ref. [21]. Lower panel: Relative difference. Dotted lines show $\lambda_{\rm c,vac}$ and $\lambda_{\rm c,wall}$.

The comparison of the curves shows that they mainly diverge by 100%, such that the approximated criterion turns out to be very weak.

VI. APPLICATIONS AND DISCUSSION

A. Chameleonic Casimir-like force

The one-dimensional configuration in Sec. IV is similar to the typical experimental setup in Casimir effect measurements in which two nearby plates experience a force of quantum origin [39,40]. In the case of the chameleon field, one expects an extra effect that would add up to the conventional Casimir force. In both cases, the force between the walls is attractive. The walls play the role of the plates, and the effect originates from the fact that the field in the walls is not symmetrical and thus its gradient does not cancel. The global behavior of the force as a function of the distance between the walls was computed with an approximate analytic model in Ref. [21].

The force a wall feels can be computed by integrating the gradient of the field over the whole wall. Knowing the profile associated with a two-wall configuration, a 1D integration gives the pressure,

$$F_s = -c^2 \frac{\beta}{M_{\rm Pl}} \int_{\frac{d}{2}}^{\frac{d}{2}+e} \nabla_x \phi \rho_{\rm wall} dx$$
$$= -c^2 \frac{\beta}{M_{\rm Pl}} \rho_{\rm wall} [\phi_d - \phi(d/2)]. \quad (19)$$

Figure 16 shows the evolution of this pressure in the case of our simulations and in the case of Ref. [21], as a function of the separation of the walls. Both curves have the same global behavior, with a plateau for small separations and an exponential suppression for separations greater than $\lambda_{\rm c,vac}$. This latter behavior is consistent with Sec. V B, as we saw that for large separations the walls can be considered as isolated, so the field tends to the symmetrical case of Sec. III B.

Despite their similar behavior, the two curves do not match perfectly. For small separations they agree within a few percent. In the intermediate regime $\lambda_{\rm c,wall} < \frac{d}{2} < \lambda_{\rm c,vac}$, they diverge by a few tenths of a percent, and for larger separations they diverge more severely. The force we find is weaker, and this might slightly relax current Casimir measurement constraints on the chameleon [21].

B. Thin- and thick-shell approximations of a ball

Another important case is a spherical uniform ball. In the chameleon's original article [16], the profile around a ball was approximated in two extremal regimes: the thick-shell regime in which the ball is too small for the field to reach the minimum of the potential in the ball; and the thin-shell regime in which the ball is large enough for the field to remain mainly at the minimum of the potential throughout most of the ball. Our simulations can provide the field around a ball in any regime.

Figure 17 compares our simulations with the thin-shell and thick-shell approximations, with different contrasts between the vacuum and the ball density (then different values of $\phi_{\rm vac}$). In the thick-shell regime, our simulation and the thick-shell model are in very good agreement (to less than a percent) when the density contrast is low. When the density contrast is larger, the agreement is even better (to less than 0.01%). In the thin-shell regime, the two profiles agree to within a few percent, except inside a zone

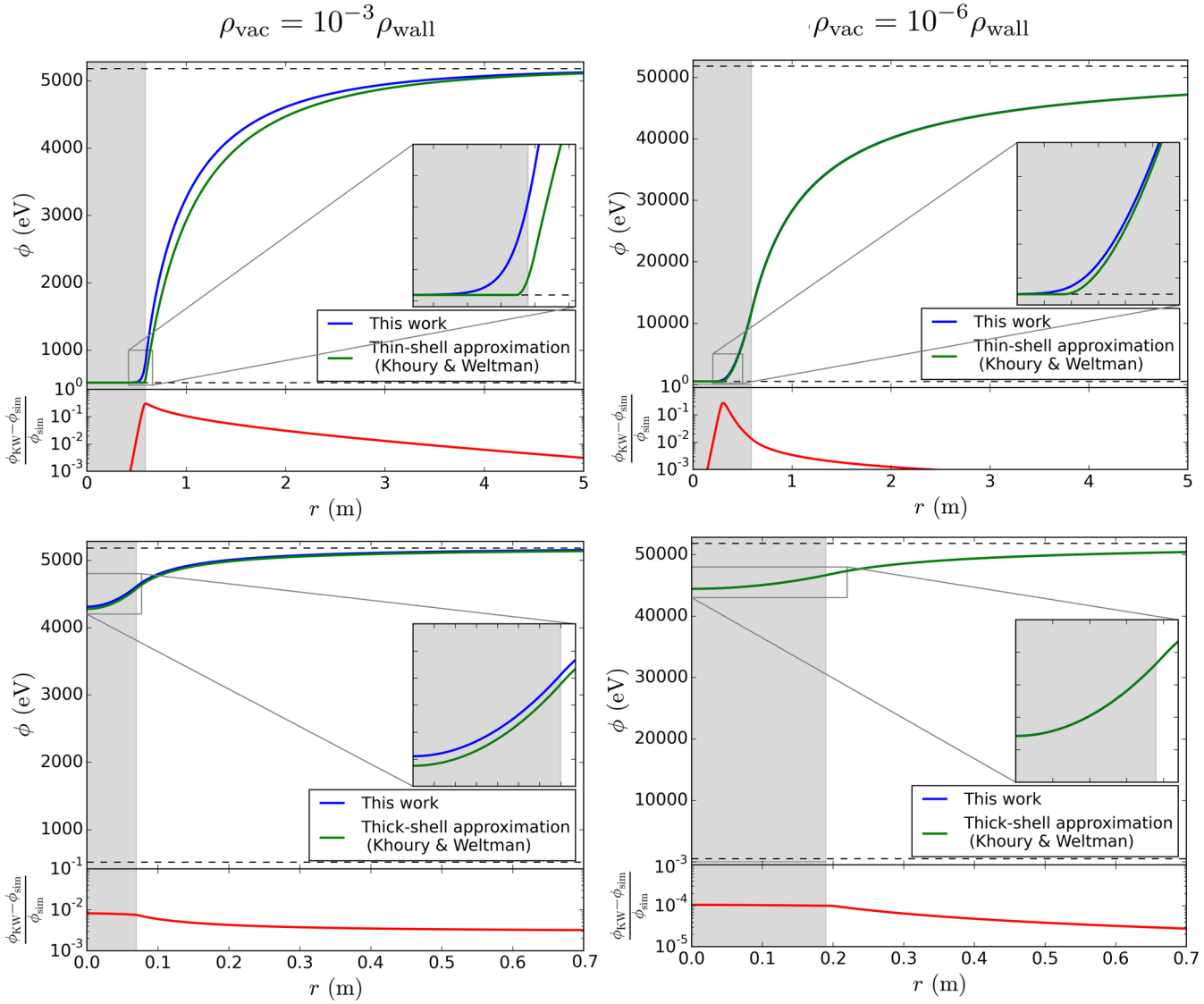

FIG. 17. Radial field profiles of a ball embedded in vacuum. The shaded zone corresponds to the inside of the ball. These simulations are compared to the models of Ref. [16] in the thin-shell regime (upper panels) and thick-shell regime (lower panels). The left and right panels correspond to different matter contrasts between the ball and the vacuum. $\phi_{\rm min}$ values are shown as dashed lines.

around the interface between the ball and the vacuum, where they agree to within a few tenths of a percent. This comes mainly from the difference in the skin depth of the wall on which the field varies. For higher density contrasts, the agreement is globally better, but there is still a slight difference where the field starts to vary inside the ball.

We can therefore assume that, except for inside the ball, the models are globally accurate in the thin-shell regime. In between the two regimes, when the ball has an intermediate radius, these two models are less accurate, particularly for low density contrasts.

C. Radial drift of test masses in a cylinder

As shown above, the chameleon inside a cavity creates a radial outward force that affects test masses (like atoms). For instance, the profile of the force created in the cylindrical case of Fig. 14 is shown in the upper panel of Fig. 18. This force may affect any experiment based on monitoring the trajectory of atoms inside a cylindrical cavity [41], even if measuring it is not the primary objective of the experiment (in which case it should be considered as a source of systematic uncertainty).

Let us consider an experiment where atoms (test masses) are dropped at a distance R_0 from the main symmetry axis of the cylinder (either alongside the axis, or radially): the atoms will experience an outward radial drift, with a drift rate depending on the parameters (β, Λ, n) of the model. For instance, in the screened cylindrical case of Fig. 14, if they are dropped with a null velocity at $R_{\rm vac}/10$, the atoms will reach the border of the cavity in 2498 s. The middle panel of Fig. 18 shows the total drift time for the atoms to reach

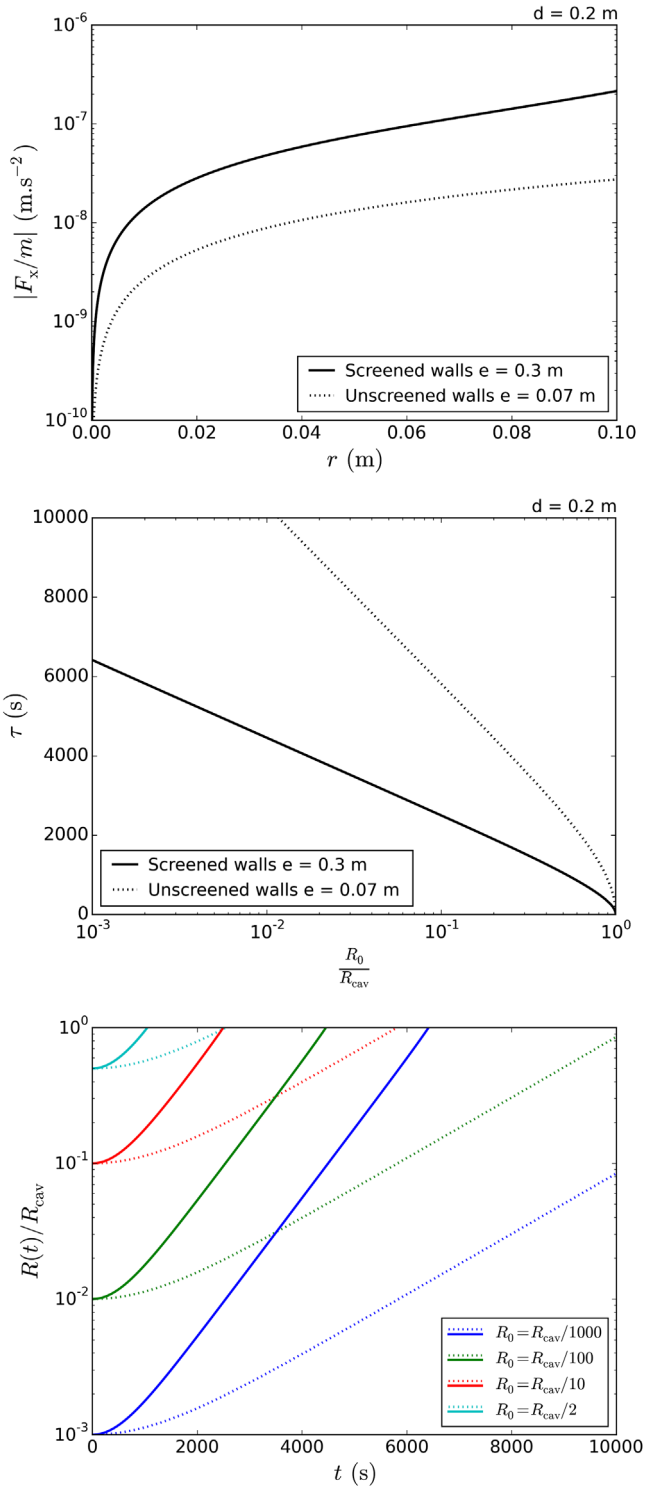

FIG. 18. Upper panel: Fifth force associated with the cylindrical cavity in Fig. 14. Middle panel: Total drift time from some initial position R_0 to the border of the cavity R_{cav}. Lower panel: Radial position of atoms R as they drift with time t for different initial positions. Solid lines correspond to screened walls ($e = 0.3$ m) and dotted lines to unscreened walls ($e = 0.07$ m).

R_{cav} as a function of R_0. In the unscreened case, as the profile is flatter, the force is weaker than in the screened case, so that the drift time is typically longer. Trivially, the smaller R_0, the longer the drift time. The lower panel shows the evolution with time t of the radial position R of atoms in the cavity for different initial positions R_0.

In more realistic setups, the drift should be estimated in view of typical integration times as it may become non-negligible, even in experiments not specifically looking for a chameleon inside the cavity. For instance, we could conceive of an experiment where the motion of atoms under the influence of the Earth's gravitational field is measured. If the chameleon force inside the cavity is strong enough to impart a detectable drift on the atoms, it should be considered as a source of systematic error (though its detection would be a significant breakthrough). Another typical case is where we drop two types of atoms, e.g., to test the equivalence principle in the Earth's gravitational field; if the chameleon coupling β is not universal, then the chameleon inside the cavity will make the atoms drift differentially, thereby mimicking a violation of the equivalence principle, though it would be considered as a systematic uncertainty on the main measurement.

D. Nested cylinders: Toward the MICROSCOPE configuration

Our computation generalizes to more complex configurations, such as the case of nested infinite cylinders. Figure 19 compares different profiles for two nested cylinders of either same or different matter densities.

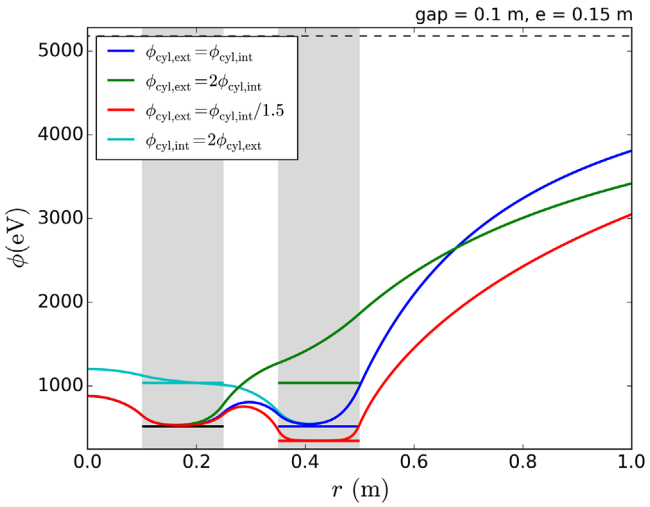

FIG. 19. Radial profiles for two nested cylinders of thickness e and different matter densities, to which correspond different values of ϕ_{min}. These ϕ_{min} values are represented by the horizontal segments. Cylinders are delimited by the shaded regions and separated by a distance gap.

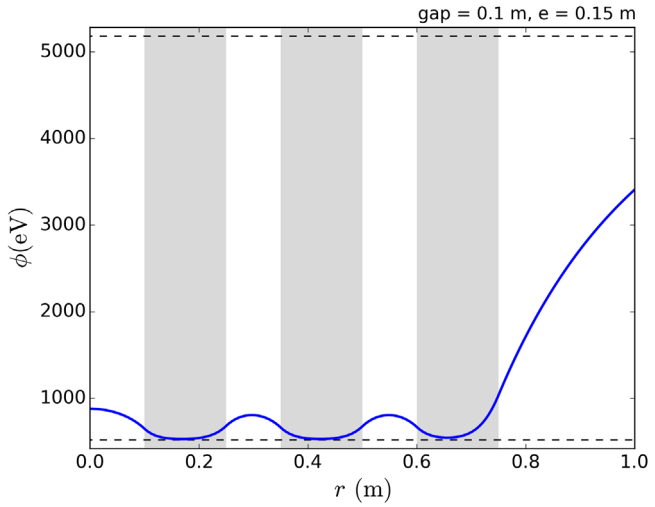

FIG. 20. Radial profile for three nested cylinders of thickness e with the same matter density. Cylinders are delimited by the shaded regions and separated by a distance *gap*. The $\phi_{\min}$ values are represented by the horizontal segments.

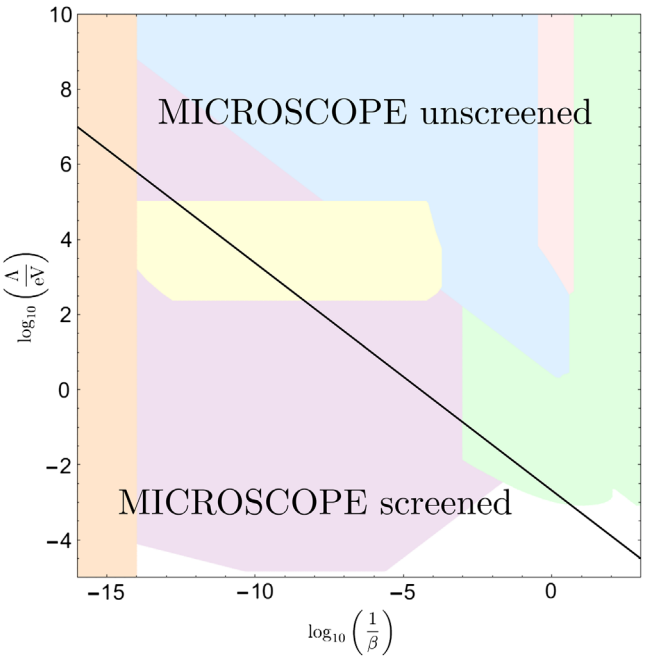

FIG. 21. The chameleon's parameter space adapted from Refs. [17,18]. The black line corresponds to parameters for which $100\lambda_{\mathrm{c,shield}} = e_{\mathrm{shield}}/2$ and delimits two regimes, i.e., whether the MICROSCOPE setup is screened or not. The colored regions correspond to current constraints from other experiments: atomic interferometry (purple [42]), Eöt-Wash (green [22,43]), Casimir effect measurements (yellow [21,44]), astrophysics tests (blue [45–47]), lensing (pink [48]), and precision atomic tests (orange [49,50]).

Consistently with our 1D study, the nature of the outer cylinder has no influence on the profile inside the inner cylinder when the cylinders are screened. Besides, in the empty inter-cylinder space, atoms experience a drift similar to the one discussed previously. But whereas in the cylindrical cavity a change in the direction in the force occurs at the center of the cavity, here it no longer occurs at the middle of the empty space but rather at some other location (at the maxima of the field) that depends on the densities of the cylinders and on the parameters of the model. This change of direction can even disappear, as it does for the green line. Then, different signatures are expected for different cylinders' features and chameleon parameters.

Figure 20 shows the radial profile obtained for three nested cylinders. This configuration is similar to the MICROSCOPE experiment's design in which cylindrical test masses are nested in cylindrical sensors. The middle cylinder experiences a chameleonic fifth force from the cylinders; nevertheless, when integrated over the whole cylinder it vanishes due to the cylindrical symmetry. We expect a force to appear when the symmetry is broken, e.g., when one of the cylinders is not perfectly centered. While this would require more intricate computations, (which will be described in a follow-up article), we can estimate the magnitude of such a force. To that purpose, we consider the force exerted on a cylindrical element (of opening angle $\mathrm{d}\theta$ and height $\mathrm{d}l$) of a cylinder. In the case shown in Fig. 20, this force is $\frac{\mathrm{d}F}{\mathrm{d}\theta\mathrm{d}l} = 6.3 \times 10^{-6}$ N m^{-1} rad^{-1}, and is directed towards the center. We expect the total force in a decentered configuration to be of the same order of magnitude up to a geometry factor.

In Ref. [16] it was claimed that MICROSCOPE could detect a clear violation of the weak equivalence principle from the chameleon field sourced by the Earth. However, the screening due to the experimental setup itself was neglected. The MICROSCOPE setup is actually enclosed in a shield of thickness $e_{\mathrm{shield}} \simeq 1$ cm. Using the screening criterion of Sec. III B 3, we show in Fig. 21 that the chameleon parameter space (for $n = 1$) is divided into two regions: above the black line (which shows where $100\lambda_{\mathrm{c,shield}} = e_{\mathrm{shield}}/2$, where $\lambda_{\mathrm{c,shield}}$ stands for the Compton wavelength associated with the shield's density) MICROSCOPE is not screened, but it is screened below the line. Thus, no violation of the weak equivalence principle can be expected below the line, while it could still be expected above it. The colored regions in Fig. 21 correspond to regions that have already been experimentally excluded [17]. It is then clear that the constraining potential of MICROSCOPE is much less than anticipated. It could only improve our current knowledge about the chameleon in a small region. This will be the subject of future work where the effect of the Earth on the chameleon profile will be included.

VII. CONCLUSION

In this article, we treated the problem of solving the chameleon scalar field's profile by paying special attention

to the boundary conditions. We found that it is possible to deal with this problem numerically without using any approximations. Our approach considers a matter system embedded in a background environment. We first considered 1D symmetrical systems. We treated the cases of a single wall and a cavity modeled as two separated walls. We determined a refined criterion which guarantees that screening occurs within a cavity. For instance, we checked that we can safely consider that the field reaches its minimum inside a matter wall, as long as the wall thickness exceeds 100 times the Compton wavelength associated with the wall matter. In this case we can consider that such a wall would screen the field. In the case of a cavity, we computed the profiles of forces that test masses would experience inside the cavity. We also computed the Casimir-like force and found discrepancies with analytic approximations in the literature. We then explored 2D and 3D symmetrical geometries. The case of a ball was compared to the thin-shell and thick-shell models from Ref. [16]. We found it to be in very good agreement, except in the region close to the ball's boundary. In a cylindrical cavity, we studied how point masses like atoms could experience a drift between the cylinders which may either lead to an experimental method of detecting chameleons or create a new source of systematic uncertainty in future experiments.

Finally, we treated the case of nested cylinders of different matter densities suited to the setup of the MICROSCOPE mission. Despite the symmetry considered here, which leads to a null force experienced by the cylinders, we provided an estimate of the magnitude of the force when the symmetry is broken. This effect will be explored by simulating nonsymmetric configurations in a follow-up article. Moreover, our analysis challenges the previous claim on the ability of space experiments to detect chameleon-sourced violations of the weak equivalence principle sourced by the Earth [15,16]. Using the refined screening criterion for cavities, we deduced that for a large region of the parameter space such an effect would be screened by the experimental setup. The Earth should be included in simulations of the remaining region. This will be the subject of a forthcoming article.

ACKNOWLEDGMENTS

We thank Manuel Rodrigues, Gilles Métris, and Pierre Touboul for useful discussions and technical information about the MICROSCOPE experiment. We thank the members of the MICROSCOPE Science Working Group for allowing us to start this project and encouraging us to pursue it. We acknowledge the financial support of CNES through the APR program ("GMscope+" project). M. P. B. is supported by a CNES/ONERA PhD grant. This work uses technical details of the T-SAGE instrument, installed on the CNES-ESA-ONERA-CNRS-OCA-DLR-ZARM MICROSCOPE mission. This work is supported in part by the EU Horizon 2020 research and innovation programme under the Marie-Sklodowska Grant No. 690575. This article is based upon work related to the COST Action CA15117 (CANTATA) supported by COST (European Cooperation in Science and Technology).

[1] C. M. Will, The confrontation between general relativity and experiment, Living Rev. Relativity **17**, 4 (2014).
[2] M. Ishak, Testing general relativity in cosmology, Living Rev. Relativity **22**, 1 (2019).
[3] LIGO Scientific and Virgo Collaborations, Observation of Gravitational Waves from a Binary Black Hole Merger, Phys. Rev. Lett. **116**, 061102 (2016).
[4] LIGO Scientific and Virgo Collaborations, Multi-messenger observations of a binary neutron Star merger, Astrophys. J. Lett. **848**, L12 (2017).
[5] Y. Akrami, F. Arroja, M. Ashdown, J. Aumont, C. Baccigalupi, M. Ballardini, A. J. Banday, R. B. Barreiro, and N. Bartolo (Planck Collaboration), Planck 2018 results. I. Overview and the cosmological legacy of Planck, arXiv:1807.06205.
[6] P. Peter and J.-P. Uzan, *Primordial Cosmology*, Oxford Graduate Texts (Oxford University Press, Oxford, 2009).
[7] B. Jain *et al.*, Novel probes of gravity and dark energy, arXiv:1309.5389.
[8] P. C. C. Freire, N. Wex, G. Esposito-Farse, J. P. W. Verbiest, M. Bailes, B. A. Jacoby, M. Kramer, I. H. Stairs, J. Antoniadis, and G. H. Janssen, The relativistic pulsarwhite dwarf binary PSR J1738 + 0333 II. The most stringent test of scalartensor gravity, Mon. Not. R. Astron. Soc. **423**, 3328 (2012).
[9] A. Riazuelo and J.-P. Uzan, Cosmological observations in scalar-tensor quintessence, Phys. Rev. D **66**, 023525 (2002).
[10] A. Coc, K. A. Olive, J.-P. Uzan, and E. Vangioni, Big bang nucleosynthesis constraints on scalar-tensor theories of gravity, Phys. Rev. D **73**, 083525 (2006).
[11] T. Damour and K. Nordtvedt, General Relativity as a Cosmological Attractor of Tensor-Scalar Theories, Phys. Rev. Lett. **70**, 2217 (1993).
[12] J.-P. Uzan, Cosmological scaling solutions of nonminimally coupled scalar fields, Phys. Rev. D **59**, 123510 (1999).
[13] T. Damour and A. Polyakov, The string dilation and a least coupling principle, Nucl. Phys. **B423**, 532 (1994).
[14] K. Hinterbichler and J. Khoury, Screening Long-Range Forces Through Local Symmetry Restoration, Phys. Rev. Lett. **104**, 231301 (2010).

[15] J. Khoury and A. Weltman, Chameleon Fields: Awaiting Surprises for Tests of Gravity in Space, Phys. Rev. Lett. **93**, 171104 (2004).
[16] J. Khoury and A. Weltman, Chameleon cosmology, Phys. Rev. D **69**, 044026 (2004).
[17] C. Burrage and J. Sakstein, Tests of chameleon gravity, Living Rev. Relativity **21**, 1 (2018).
[18] P. Brax, C. Burrage, and A.-C. Davis, Laboratory constraints, Int. J. Mod. Phys. D **27**, 1848009 (2018).
[19] C. Burrage and E. J. Copeland, Using atom interferometry to detect dark energy, Contemp. Phys. **57**, 164 (2016).
[20] D. Sabulsky, I. Dutta, E. A. Hinds, B. Elder, C. Burrage, and E. J. Copeland, Experiment to Detect Dark Energy Forces Using Atom Interferometry, Phys. Rev. Lett. **123**, 061102 (2019).
[21] P. Brax, C. van de Bruck, A.-C. Davis, D. F. Mota, and D. Shaw, Detecting chameleons through Casimir force measurements, Phys. Rev. D **76**, 124034 (2007).
[22] A. Upadhye, Dark energy fifth forces in torsion pendulum experiments, Phys. Rev. D **86**, 102003 (2012).
[23] S.-w. Chiow and N. Yu, Multiloop atom interferometer measurements of chameleon dark energy in microgravity, Phys. Rev. D **97**, 044043 (2018).
[24] P. Touboul *et al.*, Microscope Mission: First Results of a Space Test of the Equivalence Principle, Phys. Rev. Lett. **119**, 231101 (2017).
[25] P. Brax, G. Pignol, and D. Roulier, Probing strongly coupled chameleons with slow neutrons, Phys. Rev. D **88**, 083004 (2013).
[26] A. N. Ivanov, R. Höllwieser, T. Jenke, M. Wellenzohn, and H. Abele, Influence of the chameleon field potential on transition frequencies of gravitationally bound quantum states of ultracold neutrons, Phys. Rev. D **87**, 105013 (2013).
[27] C. Burrage, E. J. Copeland, and E. A. Hinds, Probing dark energy with atom interferometry, J. Cosmol. Astropart. Phys. 03 (2015) 042.
[28] C. Burrage, E. J. Copeland, and J. A. Stevenson, A proposed experimental search for chameleons using asymmetric parallel plates, J. Cosmol. Astropart. Phys. 08 (2016) 070.
[29] A. Ivanov, G. Cronenberg, R. Hllwieser, T. Jenke, M. Pitschmann, M. Wellenzohn, and H. Abele, Exact solution for chameleon field, self-coupled through the Ratra-Peebles potential with $n = 1$ and confined between two parallel plates, Phys. Rev. D **94**, 085005 (2016).
[30] T. Nakamura, T. Ikeda, R. Saito, and C.-M. Yoo, Chameleon field in a spherical shell system, Phys. Rev. D **99**, 044024 (2019).
[31] L. Kraiselburd, S. J. Landau, M. Salgado, D. Sudarsky, and H. Vucetich, Equivalence principle in chameleon models, Phys. Rev. D **97**, 104044 (2018).
[32] L. Kraiselburd, S. Landau, M. Salgado, D. Sudarsky, and H. Vucetich, Thick shell regime in the chameleon two-body problem, Phys. Rev. D **99**, 083516 (2019).
[33] P. Hamilton, M. Jaffe, P. Haslinger, Q. Simmons, H. Mller, and J. Khoury, Atom-interferometry constraints on dark energy, Science **349**, 849 (2015).
[34] B. Elder, J. Khoury, P. Haslinger, M. Jaffe, H. Mller, and P. Hamilton, Chameleon dark energy and atom interferometry, Phys. Rev. D **94**, 044051 (2016).
[35] S. Schlgel, S. Clesse, and A. Fzfa, Probing modified gravity with atom-interferometry: A numerical approach, Phys. Rev. D **93**, 104036 (2016).
[36] C. Burrage, E. J. Copeland, A. Moss, and J. A. Stevenson, The shape dependence of chameleon screening, J. Cosmol. Astropart. Phys. 01 (2018) 056.
[37] B. Ratra and P. J. E. Peebles, Cosmological consequences of a rolling homogeneous scalar field, Phys. Rev. D **37**, 3406 (1988).
[38] P. Brax, C. van de Bruck, A.-C. Davis, D. F. Mota, and D. Shaw, Testing chameleon theories with light propagating through a magnetic field, Phys. Rev. D **76**, 085010 (2007).
[39] A. O. Sushkov, W. J. Kim, D. A. R. Dalvit, and S. K. Lamoreaux, Observation of the thermal Casimir force, Nat. Phys. **7**, 230 (2011).
[40] A. Lambrecht and S. Reynaud, Casimir effect: Theory and experiments, Int. J. Mod. Phys. A **27**, 1260013 (2012).
[41] C. Llinares and P. Brax, Detecting Coupled Domain Walls in Laboratory Experiments, Phys. Rev. Lett. **122**, 091102 (2019).
[42] M. Jaffe, P. Haslinger, V. Xu, P. Hamilton, A. Upadhye, B. Elder, J. Khoury, and H. Mller, Testing sub-gravitational forces on atoms from a miniature in-vacuum source mass, Nat. Phys. **13**, 938 (2017).
[43] D. J. Kapner, T. S. Cook, E. G. Adelberger, J. H. Gundlach, B. R. Heckel, C. D. Hoyle, and H. E. Swanson, Tests of the Gravitational Inverse-Square Law Below the Dark-Energy Length Scale, Phys. Rev. Lett. **98**, 021101 (2007).
[44] R. S. Decca, D. López, E. Fischbach, G. L. Klimchitskaya, D. E. Krause, and V. M. Mostepanenko, Tests of new physics from precise measurements of the casimir pressure between two gold-coated plates, Phys. Rev. D **75**, 077101 (2007).
[45] B. Jain, V. Vikram, and J. Sakstein, Astrophysical tests of modified gravity: Constraints from distance indicators in the nearby universe, Astrophys. J. **779**, 39 (2013).
[46] A. Cabré, V. Vikram, G.-B. Zhao, B. Jain, and K. Koyama, Astrophysical tests of gravity: A screening map of the nearby universe, J. Cosmol. Astropart. Phys. 07 (2012) 034.
[47] V. Vikram, J. Sakstein, C. Davis, and A. Neil, Astrophysical tests of modified gravity: Stellar and gaseous rotation curves in dwarf galaxies, Phys. Rev. D **97**, 104055 (2018).
[48] H. Wilcox, R. C. Nichol, G.-B. Zhao, D. Bacon, K. Koyama, and A. K. Romer, Simulation tests of galaxy cluster constraints on chameleon gravity, Mon. Not. R. Astron. Soc. **462**, 715 (2016).
[49] P. Brax and C. Burrage, Atomic precision tests and light scalar couplings, Phys. Rev. D **83**, 035020 (2011).
[50] J. Jaeckel and S. Roy, Spectroscopy as a test of coulomb's law: A probe of the hidden sector, Phys. Rev. D **82**, 125020 (2010).